

Design of metasurfaces in 3D for omnidirectional band gaps: The scalar wave case

Ke Ma^a, Heedong Goh^{b,c}, Loukas F. Kallivokas^{d,*}

^a Department of Engineering Mechanics, The University of Texas at Austin, Austin, TX 78712, USA

^b Chandra Department of Electrical and Computer Engineering, The University of Texas at Austin, Austin, TX 78712, USA

^c Photonics Initiative, Advanced Science Research Center, The City University of New York, New York, NY 10017, USA

^d Oden Institute for Computational Engineering and Sciences, The University of Texas at Austin, Austin, TX 78712, USA

ARTICLE INFO

Article history:

Received 12 May 2022

Received in revised form 25 October 2022

Accepted 25 October 2022

Available online 12 November 2022

Keywords:

Omnidirectional band gaps

Acoustic metasurfaces

Inverse medium design

ABSTRACT

We discuss a comprehensive process for designing the material properties of three-dimensional periodic structures that are tasked to exhibit user-defined omnidirectional band gaps. To this end, we build upon the framework first posited in Goh and Kallivokas (2019) for two-dimensional metamaterials, and aim at engineering the dispersive properties of a metamaterial's 3D unit cell using an inverse medium approach. The inversion is driven by forcing the vanishing of trial group velocities at the target band gap frequencies, subject to the satisfaction of the Floquet–Bloch eigenvalue problem defined over the unit cell's IBZ. Omnidirectionality is controlled by enforcing the vanishing of the group velocities along the IBZ's high-symmetry lines. Using an adjoint method, the unit cell's properties are iteratively updated until the design goal is attained. Numerical examples for acoustic metamaterials and metasurfaces demonstrate the methodology.

© 2022 Elsevier Ltd. All rights reserved.

1. Introduction

The need for controlling the propagation of waves in engineered or natural systems arises commonly across the acoustics, electromagnetics, and mechanical wave regimes. Applications of interest across all regimes include cloaking [1–4], lensing [5,6], steering [7,8], shielding [9–12], band-gapping [13], and, more recently, extend to analog computing [14], with as yet untapped potential in dynamic adaptability, and cross-regime applications.

Wave control is typically accomplished by engineering the dispersive properties of periodic structures and their subperiodic derivatives (e.g., metasurfaces) to attain a user-specified design objective. Engineering the periodic assembly's properties requires that the topology, or the constituent materials, or both, be designed. To date, this is mostly done on an ad hoc basis, with only few systematic approaches appearing in the literature.

In this paper, we discuss the extension in three dimensions of a recently developed systematic procedure [15,16] for the design of acoustic metasurfaces to impart a user-defined band gap. Our approach relies on the design of the unit cell using an inverse medium constrained optimization methodology, with the unit cell's Floquet–Bloch eigenvalue problem (FBEP) acting as a constraint. Omnidirectional band gaps, i.e., metasurfaces exhibiting

band gaps independent of wave incidence are of particular interest, because of their ability to be used as filters and wave shields. In the following, we describe the methodology, complimented by numerical examples demonstrating the algorithm's success in attaining the design goals.

2. The FBEP

We are concerned with a structure that consists of periodically arranged unit cells: Fig. 1 depicts, in the reciprocal space, simple cubic, orthorhombic, and tetragonal unit cells, which could be used as the building blocks of the periodic structure. Highlighted in the same figure (red lines) are the Irreducible Brillouin Zones (IBZs) of each depicted unit cell. We appeal first to the fully-periodic problem. Accordingly, we consider the propagation of SH waves, which, in the unit cell $\Omega_{\text{cell}} \subset \mathbb{R}^3$, is governed by the three-dimensional scalar Helmholtz equation:

$$\nabla \cdot [\mu(\mathbf{x}) \nabla U(\mathbf{x})] + \omega^2 \rho(\mathbf{x}) U(\mathbf{x}) = 0, \quad \mathbf{x} \in \Omega_{\text{cell}}, \quad (1)$$

where \mathbf{x} denotes position vector, $U(\mathbf{x})$ is the anti-plane displacement, ω is circular frequency, and μ and ρ are the elastic medium's shear modulus and mass density, respectively. With these definitions, the phase velocity is defined as $c = \sqrt{\mu/\rho}$. We note that the acoustic case is governed by the same Eq. (1), subject to a reinterpretation of the physical variables: in the acoustic case U would denote total pressure, the reciprocal of μ

* Corresponding author.

E-mail addresses: kemadchsz741@utexas.edu (K. Ma), heedong.goh@utexas.edu (H. Goh), loukas@mail.utexas.edu (L.F. Kallivokas).

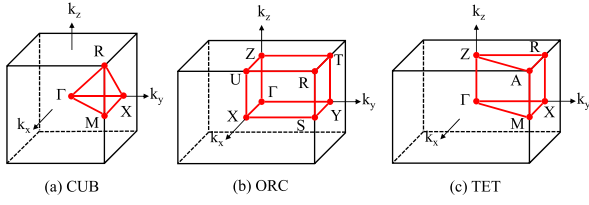


Fig. 1. Irreducible Brillouin Zones of three commonly encountered periodic structure unit cells (left-to-right: cubic, orthorhombic, tetragonal).

would be the acoustic fluid's density, while the velocity would retain its physical meaning.

We assume that the unit cells are topologically arranged in a periodic manner, as dictated by three primitive vectors $\mathbf{p}_i \in \mathbb{R}^3$, with each defining the periodicity in the i th spatial direction; then, $\forall \mathbf{x} \in \mathbb{R}^3$ and $\forall m_i \in \mathbb{Z}$,

$$\mu(\mathbf{x}) = \mu \left(\mathbf{x} + \sum_{i=1}^3 m_i \mathbf{p}_i \right), \quad \rho(\mathbf{x}) = \rho \left(\mathbf{x} + \sum_{i=1}^3 m_i \mathbf{p}_i \right). \quad (2)$$

Under the periodic hypothesis (2), the general solution to (1) is provided by the Floquet–Bloch theorem [17] as:

$$U(\mathbf{x}) = e^{i\mathbf{k} \cdot \mathbf{x}} u(\mathbf{x}), \quad (3)$$

where \mathbf{k} denotes the Floquet–Bloch wavevector, and $u(\mathbf{x})$ is a scalar displacement-like variable satisfying the same periodicity as in (2). Substituting (3) into (1) results in the strong form of the FBEP. Here, to aid the subsequent numerical procedure that rests on finite elements, we are interested in constructing the weak form of the FBEP; to this end, we introduce a test function $V(\mathbf{x})$ –counterpart to the trial solution $U(\mathbf{x})$ –, defined as:

$$V(\mathbf{x}) = e^{i\bar{\mathbf{k}} \cdot \mathbf{x}} v(\mathbf{x}), \quad (4)$$

where $\bar{[\cdot]}$ denotes complex-conjugation of the subtended quantity. We then multiply the strong form of the FBEP by $V(\mathbf{x})$, integrate over the unit cell domain Ω_{cell} , and use the divergence theorem, to arrive at:

$$P(v, u; k) \equiv a_0(v, u) + ka_1(v, u) + k^2 a_2(v, u) = 0, \quad \forall v \in \mathcal{V}, \quad (5)$$

where

$$a_0(v, u) = \int_{\Omega_{\text{cell}}} (\nabla \bar{v} \cdot \mu \nabla u - \bar{v} \omega^2 \rho u) \, d\Omega_{\text{cell}} + i \int_{\Omega_{\text{cell}}} (\nabla \bar{v} \cdot \mu \mathbf{d}_0 u - \mathbf{d}_0 \bar{v} \cdot \mu \nabla u) \, d\Omega_{\text{cell}} + \int_{\Omega_{\text{cell}}} \mathbf{d}_0 \bar{v} \cdot \mu \mathbf{d}_0 u \, d\Omega_{\text{cell}}, \quad (6a)$$

$$a_1(v, u) = i \int_{\Omega_{\text{cell}}} (\nabla \bar{v} \cdot \mu \mathbf{d} u - \mathbf{d} \bar{v} \cdot \mu \nabla u) \, d\Omega_{\text{cell}} + \int_{\Omega_{\text{cell}}} (\mathbf{d} \bar{v} \cdot \mu \mathbf{d}_0 u + \mathbf{d}_0 \bar{v} \cdot \mu \mathbf{d} u) \, d\Omega_{\text{cell}}, \quad (6b)$$

$$a_2(v, u) = \int_{\Omega_{\text{cell}}} \mathbf{d} \bar{v} \cdot \mu \mathbf{d} u \, d\Omega_{\text{cell}}. \quad (6c)$$

and

$$\mathcal{V} = \left\{ w \in H^1(\Omega_{\text{cell}}) \mid w(\mathbf{x}) = w \left(\mathbf{x} + \sum_{i=1}^3 m_i \mathbf{p}_i \right), \quad \forall \mathbf{x} \in \partial \Omega_{\text{cell}} \right\}, \quad (7)$$

with $\partial \Omega_{\text{cell}}$ denoting the boundary of Ω_{cell} .

Remarks

Table 1
CUB IBZ high-symmetry line directions (\mathbf{d}) and offset directions (\mathbf{d}_0).

Directions	\mathbf{d}	\mathbf{d}_0
Γ – M	$(1/\sqrt{2}, 1/\sqrt{2}, 0)$	$(0, 0, 0)$
Γ – X	$(0, 1, 0)$	$(0, 0, 0)$
Γ – R	$(1/\sqrt{3}, 1/\sqrt{3}, 1/\sqrt{3})$	$(0, 0, 0)$
M – R	$(0, 0, 1)$	$(\pi/p_1, \pi/p_2, 0)$
X – M	$(1, 0, 0)$	$(0, \pi/p_2, 0)$
X – R	$(1/\sqrt{2}, 0, 1/\sqrt{2})$	$(0, \pi/p_2, 0)$

- Eq. (5) fully describes the dispersive properties of the unit cell, and by extension, of the periodic structure.
- Eq. (5) is the weak form of the FBEP cast as a quadratic eigenvalue problem in the, generally, complex Floquet–Bloch wavenumber k . While it is possible to cast both the strong and the weak form of the FBEP as a linear eigenvalue problem in ω^2 , form (5) is preferred for band gap design.
- In deriving (5), we set $\mathbf{k} = k\mathbf{d} + \mathbf{d}_0$, where \mathbf{d} represents an arbitrary direction within the unit cell, and \mathbf{d}_0 represents an offset direction vector required when computing the band structure along the high-symmetry lines that are not connected to the IBZ's center (Γ). For example, Table 1 provides the values for the vectors \mathbf{d} and \mathbf{d}_0 along the high-symmetry lines of the cubic unit cell of Fig. 1(a).
- Upon solution, Eq. (5) will result in the unit cell's complex band structure and/or dispersion surfaces, for given directions \mathbf{d} in Ω_{cell} or in the IBZ. For example, using the values in Table 1, the band structure along the six high-symmetry lines Γ – X , Γ – M , Γ – R , M – R , X – M , and X – R of the tetrahedral IBZ can be readily obtained.

3. Relation between the FBEP and band gaps

A band gap \mathcal{G} is defined as the frequency range for which there are no propagating waves. Mathematically, band gaps are associated with Floquet–Bloch wavenumbers with nonzero imaginary part, i.e. with $\text{Im}\{k\} \neq 0$, $\forall \omega \in \mathcal{G}$. Despite its simplicity, such a band gap criterion is impossible to use in order to systematically drive the design of a unit cell, for, at a minimum, it requires an exhaustive search of the wavenumber space for each trial design, and lacks an adaptive mechanism for trial design updates. Thus, next, we turn to an alternate criterion, which requires that the group velocity v_g vanish within the band gap \mathcal{G} : of central importance to the sequel is the ability to connect the group velocity to the FBEP. To this end, we appeal to the Hellman–Feynman theorem and replace v with u in (5), and, then differentiate the resulting expression with respect to the wavenumber k ; there results [15]:

$$0 = \frac{\partial}{\partial k} P(u, u; k) = 2\omega \frac{\partial \omega}{\partial k} a_{0,2}(u, u) + a_1(u, u) + 2ka_2(u, u) + 2\text{Re} \left\{ a_{0,0} \left(\frac{\partial u}{\partial k}, u \right) \right\} + 2\omega^2 \text{Re} \left\{ a_{0,2} \left(\frac{\partial u}{\partial k}, k \right) \right\} + 2k \text{Re} \left\{ a_1 \left(\frac{\partial u}{\partial k}, u \right) \right\} + 2k^2 \text{Re} \left\{ a_2 \left(\frac{\partial u}{\partial k}, u \right) \right\}. \quad (8)$$

In the above,

$$a_{0,2}(v, u) = - \int_{\Omega_{\text{cell}}} \bar{v} \rho u \, d\Omega_{\text{cell}} \quad \text{and} \quad (9a)$$

$$a_{0,0}(v, u) = a_0(v, u) - \omega^2 a_{0,2}(v, u). \quad (9b)$$

Assuming $\partial u / \partial k \in \mathcal{V}$, we take the real part of the (8) and obtain

$$v_g \equiv \frac{\partial \omega}{\partial k} = -\frac{a_1(u, u) + 2 \operatorname{Re}\{k\} a_2(u, u)}{2 \omega a_{0,2}(u, u)}. \quad (10)$$

Eq. (10) is the necessary ingredient for the systematic design of the unit cell of periodic structures and metasurfaces, for it is the *glue* between the dispersive properties of the medium (as expressed by the FBEP) and the design objective – the band gap (as expressed by the vanishing of the group velocity). In effect, the connection between the FBEP (5) and v_g afforded by (10) allows for far more general design objectives than band gaps, by, for example, allowing the tailoring of parts of the spectrum to slow or fast group velocities, as an application may warrant.

4. Periodic structure and metasurface design

To drive the unit cell design, we adopt an inverse medium methodology and define a Lagrangian L , comprising an objective functional M that encompasses the design objective, and the side imposition of the FBEP to account for the underlying physics. The steps were first described in [15], and are repeated here for completeness. Accordingly, let:

$$L[u, k, v, \xi; \rho, \mu] = M[u, k; \rho, \mu] + E[u, k, v, \xi; \rho, \mu], \quad (11a)$$

$$M[u, k; \rho, \mu] = \sum_{\alpha}^{N_{\text{freq}}} \sum_{\beta}^{N_{\text{dir}}} \sum_{\gamma}^{N_{\text{mode}}} \frac{1}{2} v_{g, \alpha \beta \gamma}^2, \quad (11b)$$

$$E[u, k, v, \xi; \rho, \mu] = \sum_{\alpha}^{N_{\text{freq}}} \sum_{\beta}^{N_{\text{dir}}} \sum_{\gamma}^{N_{\text{mode}}} \left[\operatorname{Re}\{P(v, u; k)\} + \frac{\xi}{2} \{a_2(u, u) - 1\}_{\alpha \beta \gamma} \right], \quad (11c)$$

where N_{freq} denotes the number of discrete circular frequencies within the band gap \mathcal{G} ; N_{mode} denotes the number of modes; and N_{dir} is the number of directions along which the band gap should be attained. For omnidirectional band gaps, directions along all symmetry lines of the IBZ should be considered. Eq. (11c) is the side-imposed FBEP, enhanced with an orthonormality condition to ensure the uniqueness of the eigenfunctions. Specifically, in (11c), the u, k are the eigenfunction and eigenvalue of the forward FBEP, respectively, while v, ξ denote the adjoint eigenfunction and the adjoint eigenvalue, respectively. The term $v_{g, \alpha \beta \gamma}$ in the objective functional M of (11b) denotes the group velocity corresponding to a circular frequency ω_a , a direction \mathbf{d}_β , and a mode γ , for trial distributions of the material parameters μ and ρ . The band gap design goal can then be cast as the minimization statement: find $\rho \in \mathcal{W}$ and $\mu \in \mathcal{W}$ such that

$$\min L[u, k, v, \xi; \rho, \mu] \quad (12)$$

where

$$\mathcal{W} = \left\{ w \in H^0(\Omega_{\text{cell}}) \mid w(\mathbf{x}) = w \left(\mathbf{x} + \sum_{i=1}^3 m_i \mathbf{p}_i \right), \forall \mathbf{x} \in \partial \Omega_{\text{cell}} \right\} \quad (13)$$

To solve the dispersion-constrained inverse problem (12), we seek to satisfy the first-order optimality conditions, which result in the triad of a state, adjoint, and control problems. Accordingly:

1. *State problem - forward FBEP*: given trial design variables $\rho \in \mathcal{W}$ and $\mu \in \mathcal{W}$, find state variables $u \in \mathcal{V} \setminus \{0\}$ and $k \in \mathbb{C}$ such that

$$P(k)(\tilde{v}, u) = 0, \quad \forall \tilde{v} \in \mathcal{V}, \quad (14a)$$

$$\frac{\tilde{\xi}}{2} \{a_2(u, u) - 1\} = 0, \quad \forall \tilde{\xi} \in \mathbb{R}. \quad (14b)$$

2. *Adjoint problem*: given the solutions to the state problem $u \in \mathcal{V} \setminus \{0\}$ and $k \in \mathbb{C}$, and trial design variables $\rho \in \mathcal{W}$ and $\mu \in \mathcal{W}$, find adjoint variables $v \in \mathcal{V}$ and $\xi \in \mathbb{R}$ such that

$$P(v, \tilde{u}; k) + \xi a_2(u, \tilde{u}) = (A - B) v_g, \quad \forall \tilde{u} \in \mathcal{V} \quad (15a)$$

$$\tilde{k} a_1(v, u) + 2k \tilde{k} a_2(v, u) = C v_g, \quad \forall \tilde{k} \in \mathbb{C}, \quad (15b)$$

where

$$A = \frac{a_1(u, \tilde{u}) + 2 \operatorname{Re}\{k\} a_2(u, \tilde{u})}{\omega a_{0,2}(u, u)}, \quad (16a)$$

$$B = \frac{a_1(u, u) + 2 \operatorname{Re}\{k\} a_2(u, u)}{\omega [a_{0,2}(u, u)]^2} a_{0,2}(u, \tilde{u}), \quad (16b)$$

$$C = \frac{\tilde{k} a_2(u, u)}{\omega a_{0,2}(u, u)}. \quad (16c)$$

3. *Control problem*: given the state solutions $u \in \mathcal{V} \setminus \{0\}$ and $k \in \mathbb{C}$, the adjoint solutions $v \in \mathcal{V}$ and $\xi \in \mathbb{R}$, and trial design variables $\rho \in \mathcal{W}$ and $\mu \in \mathcal{W}$, the Gâteaux derivatives of L with respect to the design variables ρ and μ become:

$$\delta_{\rho} L[\dots](\tilde{\rho}) = \delta_{\rho} M[\dots](\tilde{\rho}) + \delta_{\rho} E[\dots](\tilde{\rho}), \quad (17a)$$

$$\delta_{\mu} L[\dots](\tilde{\mu}) = \delta_{\mu} M[\dots](\tilde{\mu}) + \delta_{\mu} E[\dots](\tilde{\mu}), \quad (17b)$$

where

$$\delta_{\rho} M[\dots](\tilde{\rho}) = D \left(- \int_{\Omega_{\text{cell}}} \tilde{u} \tilde{\rho} u \, d\Omega_{\text{cell}} \right) v_g, \quad (18a)$$

$$\delta_{\rho} E[\dots](\tilde{\rho}) = \operatorname{Re} \left\{ - \int_{\Omega_{\text{cell}}} \tilde{v} \tilde{\rho} \omega^2 u \, d\Omega_{\text{cell}} \right\}, \quad (18b)$$

$$\delta_{\mu} M[\dots](\tilde{\mu}) = -(F + G) v_g, \quad (18c)$$

$$\begin{aligned} \delta_{\mu} E[\dots](\tilde{\mu}) = & \operatorname{Re} \left\{ \int_{\Omega_{\text{cell}}} \nabla \tilde{v} \cdot \tilde{\mu} \nabla u \, d\Omega_{\text{cell}} \right\} \\ & + \operatorname{Re} \left\{ ik \int_{\Omega_{\text{cell}}} (\nabla \tilde{v} \cdot \tilde{\mu} \mathbf{d}u - \mathbf{d}\tilde{v} \cdot \tilde{\mu} \nabla u) \, d\Omega_{\text{cell}} \right\} \\ & + \operatorname{Re} \left\{ k^2 \int_{\Omega_{\text{cell}}} \tilde{v} \tilde{\mu} u \, d\Omega_{\text{cell}} + \frac{\xi}{2} \int_{\Omega_{\text{cell}}} \tilde{u} \tilde{\mu} u \, d\Omega_{\text{cell}} \right\}, \end{aligned} \quad (18d)$$

with

$$D = \frac{a_1(u, u) + 2 \operatorname{Re}\{k\} a_2(u, u)}{2 \omega [a_{0,2}(u, u)]^2}, \quad (19a)$$

$$F = \frac{i \int_{\Omega_{\text{cell}}} (\nabla \tilde{u} \cdot \tilde{\mu} \mathbf{d}u - \mathbf{d}\tilde{u} \cdot \tilde{\mu} \nabla u) \, d\Omega_{\text{cell}}}{2 \omega a_{0,2}(u, u)}, \quad (19b)$$

$$G = \frac{2 \operatorname{Re}\{k\} \int_{\Omega_{\text{cell}}} \tilde{u} \tilde{\mu} u \, d\Omega_{\text{cell}}}{2 \omega a_{0,2}(u, u)}. \quad (19c)$$

In the above, the summation over the frequencies, directions, and modes is implied, but has been omitted to reduce notational congestion.

We use standard Lagrange-family approximations for the state $u(\mathbf{x})$ and adjoint $v(\mathbf{x})$ eigenfunctions, and solve first the forward FBEP (14) using an initial guess for the properties $\mu(\mathbf{x})$ and $\rho(\mathbf{x})$ of the unit cell. Next, using the state eigenpair (u, k) and the trial properties, we compute group velocities at the N_{freq} gap frequencies, and use them to drive the adjoint problem (15). Then, armed with the state and adjoint eigenpairs, we compute the Lagrangian's reduced gradient components (18), which are subsequently used in a conjugate gradient method [18], enhanced with a backtracking algorithm [19], in order to drive the material property updates. The updated material properties are then used in the next iteration of the problem triad; we consider that the

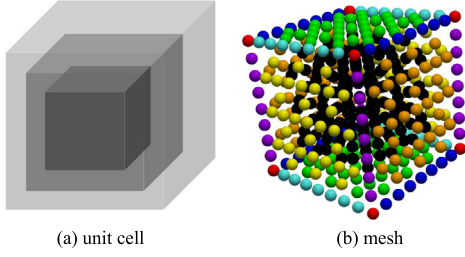


Fig. 2. (a) Unit cell geometry; (b) sample unit cell finite element mesh using 20-noded hexahedral elements (only the nodes are shown).

process converged when the objective functional M_i at the i th iteration satisfies:

$$\varepsilon_i = \frac{|M_i - M_{i-1}|}{|M_0|} < \delta_{\text{tol}}, \quad (20)$$

where δ_{tol} is a tolerance, usually set to 10^{-6} in our numerical experiments. The inverse-medium-inspired design methodology is summarily captured in Algorithm 1.

Algorithm 1 Inverse metasurface design

```

Define the unit cell (geometry, properties, IBZ, etc.)
Define the target band gap  $\mathcal{G}$ 
Set initial guess for the material properties  $\rho_0$  and  $\mu_0$ 
Initialize the iteration counter  $i \leftarrow 0$ 
Set  $\varepsilon_0 = 1$ 
while  $\varepsilon_i > \delta_{\text{tol}}$  do
  Use  $\rho_i, \mu_i$  to solve the forward FBEP (14)
  Evaluate group velocities  $v_g$  along  $\mathcal{G}$ 
  Solve the adjoint eigenvalue problem (15)
  Compute the Lagrangian's reduced gradient (18)
  Use the reduced gradient to update the material properties
  to  $\rho_{i+1}$  and  $\mu_{i+1}$  using backtracking algorithm; stop if
  sufficient-decrease condition is violated
  Set  $i \leftarrow i + 1$ 
  compute  $M_i$ ; compute  $\varepsilon_i$ 
end while

```

We note that while the described process is aimed at the design of a unit cell under infinite periodicity assumptions, it is equally applicable to metasurfaces without any appreciable modification.

5. Numerical experiments

To demonstrate the methodology, we use a cubic unit cell consisting of three concentric cubes with sides 6.0 m, 4.8 m, 3.6 m, for the outer, middle, and inner cube, respectively, as shown in Fig. 2(a); Fig. 2(b) depicts a representative finite element mesh. Each of the three concentric cubes is composed of a different material. We consider two possible material arrangements, one consisting of an initial soft-hard-soft (S-H-S) distribution, and a second one consisting of an initial hard-soft-hard (H-S-H) material configuration.

5.1. Periodic structures with omnidirectional band gaps

In the first case (S-H-S), the initial densities have all been set to 3000 kg/m^3 for all three concentric cubes of the unit cell, while the shear moduli have been set to 30 MPa for the inner and outer cubes, and to 30 GPa for the middle cube. In the second case (H-S-H), the initial densities and shear moduli have been

set to 8000 kg/m^3 and 80 GPa for the inner and outer cubes, respectively, and to 1000 kg/m^3 and 80 MPa for the middle core.

In the S-H-S case we drive the unit cell design by requiring that an omnidirectional band gap be attained in the range of 70–120 rad/s, while in the H-S-H we require that an omnidirectional band gap be realized in the 220–250 rad/s range. To effect the omnidirectional gap, we drive the inversion using only three out of the six IBZ high-symmetry lines ($N_{\text{dir}} = 3$), namely along directions $\Gamma-X$, $\Gamma-M$, and $\Gamma-R$, since they were proven to be sufficient for inversion. We note that the number of modes N_{mode} varies, as it depends on the circular frequency and the number of wavenumbers computed per frequency.

To effect the omnidirectional target band gap, we use a continuation scheme. For example, for the 70 to 120 rad/s target gap of the S-H-S case, we use a five-stage process, whereby the inversion is first driven by a narrower 70–80 rad/s target gap; once converged, the converged properties are then used as initial guesses to drive a wider gap during the next stage by opening the previous-stage gap each time by 10 rad/s, i.e., from 70 to 90 rad/s, then from 70 to 100 rad/s, and so on and so forth. Fig. 3 depicts the convergence of the densities and shear moduli for the S-H-S case (left column), and for the H-S-H case (right column) during a 5- and 3-stage continuation scheme, respectively. The last row in Fig. 3 shows the convergence of the objective functional, which exhibits a 9- to 11-order reduction from the initial guess. Also shown along the right edge of the plots in the same figure are the converged material property values: for the S-H-S case, and from the inner to the outer cube, they are 6530 kg/m^3 , 4377 kg/m^3 , 3328 kg/m^3 for the densities, and 39 MPa, 30 GPa, and 14 MPa for the shear moduli. Similarly, for the H-S-H case, the corresponding values are 6735 kg/m^3 , 37 kg/m^3 , 7855 kg/m^3 for the densities, and 80 GPa, 95 MPa, and 80 GPa for the shear moduli.

Fig. 4(a) depicts the band structure drawn along all the IBZ high-symmetry lines for the initial properties (purple square), an intermediate inversion stage (blue circles), and the final properties (green diamond) of the S-H-S case. The shaded area is the target band gap (70–120 rad/s), and, as it can be seen, it is attained by the final-stage properties. Similarly, Fig. 4(b) shows the band structure's evolution during the inversion iterations for the H-S-H case and for a target band gap (shaded) in the 220–250 rad/s range. We note that, as is customary, the band structure is shown along the high-symmetry lines only; a more complete picture is offered in Fig. 5, which depicts a slice of the four-dimensional dispersion surface for the S-H-S case along the (k_x, k_y) plane, and clearly shows the attained gap. We note that the process can also accommodate multiple gaps: consider the same three-material design, with initial densities of 3000 kg/m^3 for all cubes, and shear moduli of 30 MPa, 30 GPa, and 30 MPa, driven by two gaps set at 70–90 rad/s and 120–140 rad/s. Fig. 6 depicts the initial and final band structure, showing that the target gaps have been realized; to attain the two gaps, the moduli were only slightly changed, whereas the final density values were 9780 kg/m^3 , 5143 kg/m^3 , and 3942 kg/m^3 , respectively.

5.2. A metasurface with an omnidirectional band gap

The numerical examples of the preceding section are predicated on the assumption of infinite periodicity. Of interest herein is whether the converged designs can be used to realize a metasurface without significant loss of their intended functionality, i.e., to still realize an omnidirectional band gap at the targeted frequency ranges. To test the hypothesis, we embed a single-cell-high metasurface in a background host with density 3000 kg/m^3 and shear modulus of 30 MPa. As shown in Fig. 7, the metasurface is assumed to be periodic in the x and y directions, while it

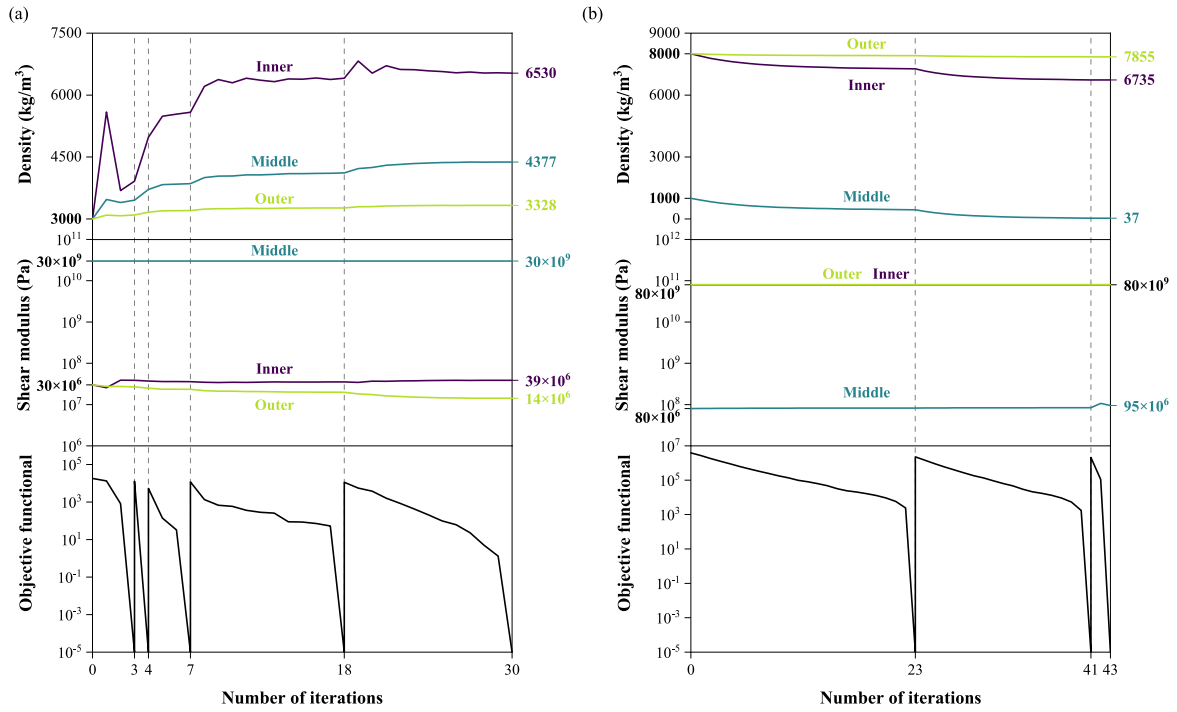


Fig. 3. Material properties and objective functional M convergence; left column: S-H-S case; right column: H-S-H case.

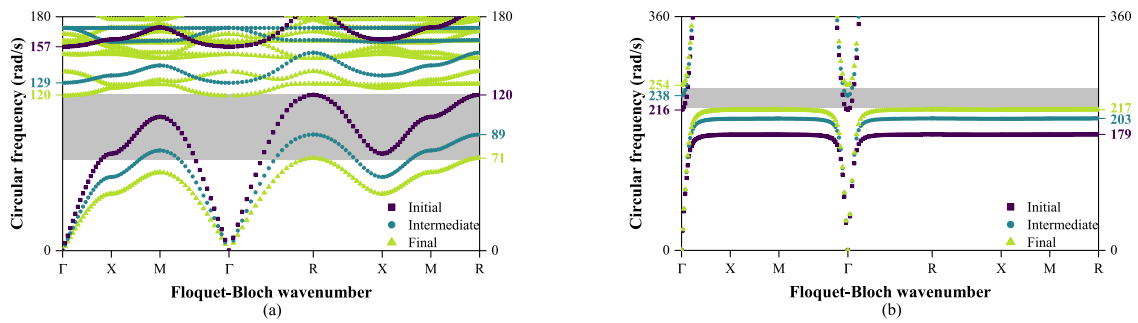


Fig. 4. Evolution of band structure during inversion iterations; left: S-H-S case; target gap at 70–120 rad/s; right: H-S-H case; target gap at 220–250 rad/s; the band gaps are shown as shaded areas.

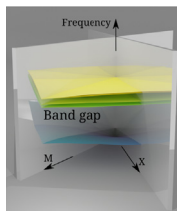


Fig. 5. S-H-S case dispersion surfaces.

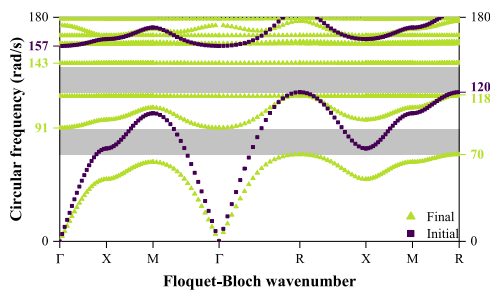


Fig. 6. Initial and final band structure, for a 2-band-gap design.

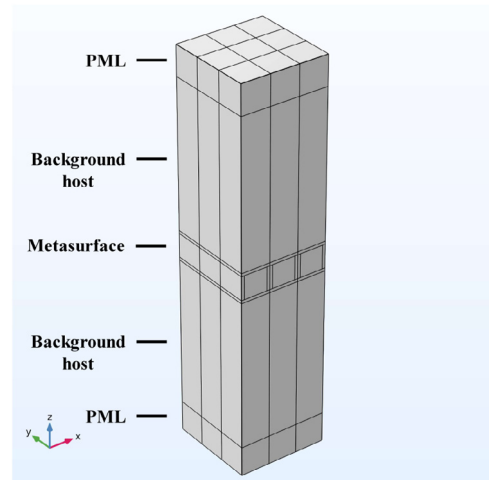


Fig. 7. A single-cell-high metasurface embedded in a background host.

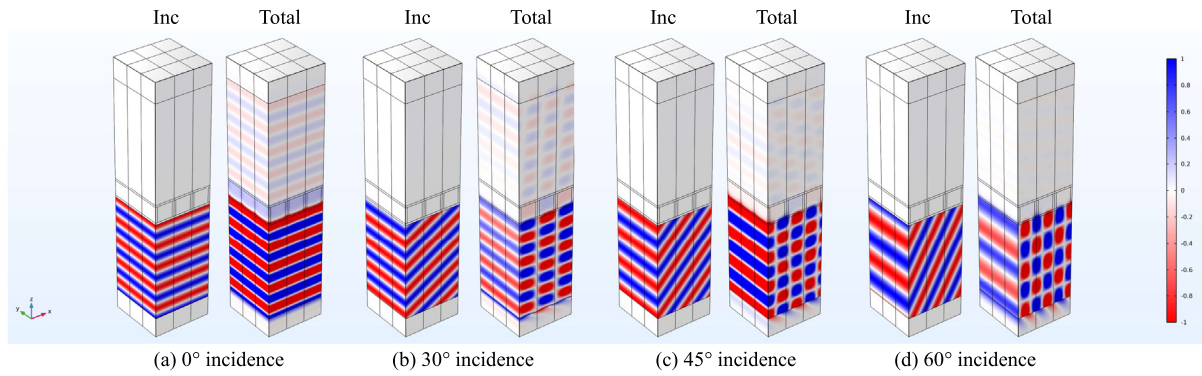


Fig. 8. Performance of a metasurface when insonified by a monochromatic incident plane wave of 95 rad/s at various angles of incidence; left-to-right: incident and total motion at 0°, 30°, 45° and 60° incidence; for each pair the left column shows the incident field, and the right column shows the total field.

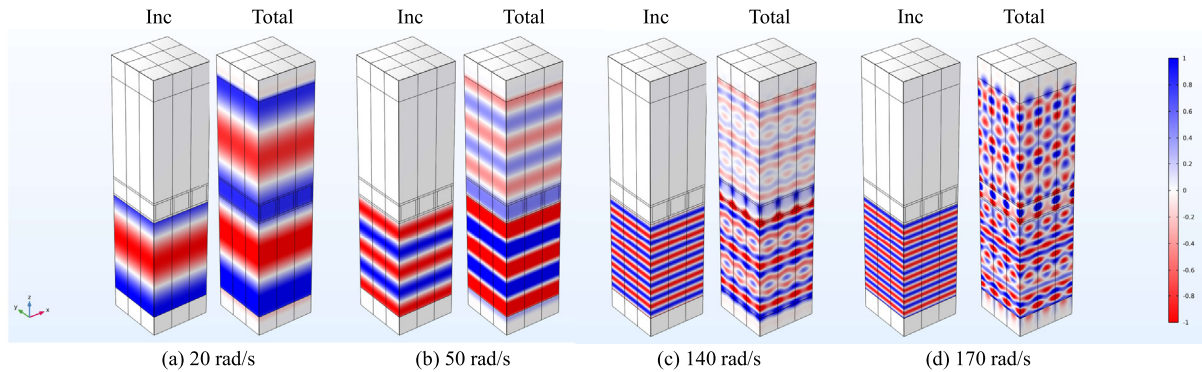


Fig. 9. Performance of a metasurface when insonified by monochromatic vertically incident plane waves at non-band-gap frequencies; left-to-right: 20 rad/s, 50 rad/s, 140 rad/s and 170 rad/s; for each pair the left column shows the incident field, and the right column shows the total field.

consists of only a single cell along the z direction. The cells' properties are borrowed from the S–H–S case of the preceding section, which resulted in an omnidirectional band gap in the 70–120 rad/s range. The background host's domain is terminated with Perfectly-Matched-Layers (PMLs). We note that for simulation purposes it would have been sufficient to model a single column of the PML–host–metasurface–host–PML ensemble, but, instead, chose to model a 9-column ensemble for visualization purposes. Floquet–Bloch periodicity conditions have been applied to all lateral surfaces, and the general-purpose finite element package [20] was used for the simulations.

To test the metasurface's band-gapping omnidirectional capabilities we subject the metasurface to a monochromatic incident plane wave emanating from the lower section of the background host and impinging upon the unit cells at various angles of incidence, namely at 0° (vertical incidence), 30°, 45°, and 60° degrees. We observe the response at the forward scatter region, i.e., north of the metasurface. The frequency is set at 95 rad/s, which corresponds to the central frequency of the design band gap. Fig. 8 shows the response for the four incidence angles: for each angle, the associated pair 9-column-ensembles depicts the incident field (left) and the total field (right). As it can be seen, the metasurface has successfully arrested the propagation of the plane wave at all angles of incidence, attesting to its omnidirectional capabilities; we note that there is weak motion penetration in the forward scatter region for 0° and 30° incidence were to consist of two cells. In contrast, when the metasurface is subjected to plane waves operating at frequencies outside the gap, the metasurface will allow passage, as shown in Fig. 9 for vertical incidence at 20, 50, 140, and 170 rad/s.

6. Conclusions

We discussed a comprehensive procedure for designing the material properties of periodic structures in three dimensions in order to realize user-defined band gap targets. The presented systematic procedure rests on a dispersion-constrained inverse medium problem. Numerical experiments demonstrated the methodology's versatility in producing omnidirectional band gaps that are otherwise hard-to-realize by ad hoc procedures. Extensions of the methodology to encompass topological optimization in addition to, or at the exclusion of, material optimization are possible [21]. In this case, the Lagrangian would remain the same as the one we introduced herein, the geometry would be parameterized, and the only modification would affect the control problem, which will now rest on derivatives with respect to the parameters of the unit cell's geometry. Such geometric parameterization can be efficiently handled and benefit from the increased continuity afforded by B-Splines or NURBS [22,23].

CRedit authorship contribution statement

Ke Ma: Conceptualization, Methodology, Software. **Heedong Goh:** Conceptualization, Methodology, Software. **Loukas F. Kallivokas:** Conceptualization, Methodology.

Declaration of competing interest

The authors declare that they have no known competing financial interests or personal relationships that could have appeared to influence the work reported in this paper.

Data availability

No data was used for the research described in the article.

Acknowledgments

The work of the first author has been supported by a 2020 ConTex collaborative grant (award number 2020-43). The support of the University of Texas System, USA and CONACYT, Mexico is gratefully acknowledged.

References

- [1] A. Alù, N. Engheta, Achieving transparency with plasmonic and metamaterial coatings, *Phys. Rev. E* 72 (2005) 016623.
- [2] D. Schurig, J.J. Mock, B. Justice, S.A. Cummer, J.B. Pendry, A.F. Starr, D.R. Smith, Metamaterial electromagnetic cloak at microwave frequencies, *Science* 314 (2006) 977–980.
- [3] A.N. Norris, Acoustic cloaking theory, *Proc. R. Soc. A: Math. Phys. Eng. Sci.* 464 (2008) 2411–2434.
- [4] M. Brun, S. Guenneau, A.B. Movchan, Achieving control of in-plane elastic waves, *Appl. Phys. Lett.* 94 (2009) 061903.
- [5] J.B. Pendry, Negative refraction makes a perfect lens, *Phys. Rev. Lett.* 85 (3966) (2000).
- [6] C. Luo, S.G. Johnson, J. Joannopoulos, J. Pendry, Subwavelength imaging in photonic crystals, *Phys. Rev. B* 68 (2003) 045115.
- [7] J.B. Pendry, A. Aubry, D. Smith, S.A. Maier, Transformation optics and subwavelength control of light, *Science* 337 (2012) 549–552.
- [8] X. Su, Z. Lu, A.N. Norris, Elastic metasurfaces for splitting SV-and P-waves in elastic solids, *J. Appl. Phys.* 123 (2018) 091701.
- [9] S. Krödel, N. Thomé, C. Daraio, Wide band-gap seismic metastructures, *Extreme Mech. Lett.* 4 (2015) 111–117.
- [10] F. Meseguer, M. Hologado, D. Caballero, N. Benaches, J. Sanchez-Dehesa, C. López, J. Linares, Rayleigh-wave attenuation by a semi-infinite two-dimensional elastic-band-gap crystal, *Phys. Rev. B* 59 (12169) (1999).
- [11] M. Miniaci, A. Krushynska, F. Bosia, N.M. Pugno, Large scale mechanical metamaterials as seismic shields, *New J. Phys.* 18 (2016) 083041.
- [12] A. Colombi, D. Colquitt, P. Roux, S. Guenneau, R.V. Craster, A seismic metamaterial: The resonant metawedge, *Sci. Rep.* 6 (2016) 1–6.
- [13] C. Poulton, A. Movchan, R. McPhedran, N. Nicorovici, Y. Antipov, Eigenvalue problems for doubly periodic elastic structures and phononic band gaps, *Proc. R. Soc. Lond. Ser. A Math. Phys. Eng. Sci.* 456 (2000) 2543–2559.
- [14] H. Goh, A. Alù, Nonlocal scatterer for compact wave-based analog computing, *Phys. Rev. Lett.* 128 (2022) 073201.
- [15] H. Goh, L.F. Kallivokas, Group velocity-driven inverse metamaterial design, *J. Eng. Mech.* 145 (2019) 04019094, [http://dx.doi.org/10.1061/\(ASCE\)EM.1943-7889.0001688](http://dx.doi.org/10.1061/(ASCE)EM.1943-7889.0001688).
- [16] H. Goh, L.F. Kallivokas, Inverse band gap design of elastic metamaterials for P and SV wave control, *Comput. Methods Appl. Mech. Engrg.* 370 (2020) 113263, <http://dx.doi.org/10.1016/j.cma.2020.113263>.
- [17] N.W. Ashcroft, N.D. Mermin, *Solid State Physics*, Holt, Rinehart and Winston, New York, 1976.
- [18] R. Fletcher, Function minimization by conjugate gradients, *Comput. J.* 7 (1964) 149–154, <http://dx.doi.org/10.1093/comjnl/7.2.149>.
- [19] A. Quarteroni, R. Sacco, F. Saleri, *Numerical mathematics*, in: *Number 37 in Texts in Applied Mathematics*, second ed., Springer, Berlin, New York, 2007.
- [20] COMSOL, Multiphysics[®], V. 5.6, COMSOL AB, Stockholm, Sweden, www.comsol.com.
- [21] H. Goh, *Inverse Design of Metamaterials for Wave Control* (Ph.D. thesis), 2020, <http://dx.doi.org/10.26153/tsw/9196>.
- [22] A. Masud, R. Kannan, B-splines and NURBS based finite element methods for Kohn–Sham equations, *Comput. Methods Appl. Mech. Engrg.* 241 (2012) 112–127.
- [23] A. Masud, A.A. Al-Naseem, R. Kannan, H. Gajendran, B-splines and NURBS based finite element methods for strained electronic structure calculations, *J. Appl. Mech.* 85 (2018) 091009.